Electronic Supplementary Material (ESI) for Journal of Materials Chemistry A.

Earthworm-like N, S-Doped Carbon Tube- Encapsulated Co_9S_8 Nanocomposites Derived from Nanoscaled Metal-Organic Frameworks for Highly Efficient Bifunctional Oxygen Catalysis

Tao Liu, Limin Zhang,* and Yang Tian*

Department of Chemistry, School of Chemistry and Molecular Engineering, East China Normal University, Dongchuan Road 500, Shanghai 200241, China.

Corresponding authors: lmzhang@chem.ecnu.edu.cn, ytian@chem.ecnu.edu.cn.

Contents

1. Experimental section.

Reagents and Materials

Benzoic acid (99.5%), zirconium Chloride (98%), and thiourea (99%) were purchased from Aladdin Chemicals Company (China). Cobalt chloride hexahydrate (99.99%), hydrofluoric acid (40%), *n*-hexane, methanol (>99.7%), ethanol (>99.7%), N, N-dimethylformamide (>99.8%), 2-amino-1, 4-benzenedicarboxylic acid (99%) were bought from Sigma-Aldrich. Ultra-pure water with a specific resistance of 18.2 MΩ cm was obtained by reverse osmosis followed by ion-exchange and filtration (RFD 250NB, Toyo Seisakusho Kaisha, Ltd., Japan). Pt/C (20 wt %) (HiSPEC 2000) and ruthenium dioxide for electrochemical measurements were purchased from Johnson Matthey company. All chemicals were from commercial and used without further purification

Methods

Scanning electron microscopy (SEM) images were taken using a field mission gun Hitachi S-4800 scanning electron microscope (Japan). Transmission electron microscopy (TEM images were obtained on a Hitachi S-3400N transmission electron microscope. X-ray photoelectron spectroscopy (XPS) was conducted in PHI-5000 CESCA system (PerkinElmer). Nitrogen adsorption-desorption isotherm was collected on Autosorb iQ Station 2 at 77 K. Pore size distribution of the materials were derived from the Barrett-Joyner-Halenda (BJH) model using the adsorption branch on the isotherm and The pore volumes were calculated by a single point method at P/P_0=0.99. The Raman measurements were performed on the Thermo Scientific DXR Raman Microscope. Power X-ray diffraction (PXRD) were carried out on a Rigaku Ultima IV X-ray diffractometer with Cu Kα radiation.

Density function theory (DFT) method

Density function theory calculation were performed by using the CP2K package.[S1] PBE functional with Grimme D3 correction was used to describe the systemm.[S2,S3] Unrestricted Kohn-Sham DFT has been used as the electronic structure method in the framework of the

Gaussian and plane waves method.[S4,S5] The Goedecker-Teter-Hutter (GTH) pseudopotentials,[S6,S7]DZVP-MOLOPT-GTH basis sets were utilized to describe the molecules.[S4] A plane-wave energy cut-off of 500 Ry has been employed.The simulation is carried out in a three-dimensional periodic boundary box of 12.76x14.73x20 Angstrom^3.The Gibbs free energy is calculated using

$$\Delta G = E_{DFT} + \Delta ZPE - T\Delta S + C_v\Delta T \quad (S1)$$

Where G is Gibbs free energy, E_{DFT} the electronic energy from DFT calculations, ZPE is zeropoint-energy and C_v is the heat capacity, T is temperature of 298K.

2. SEM and TEM images of UiO-66-NH_2.

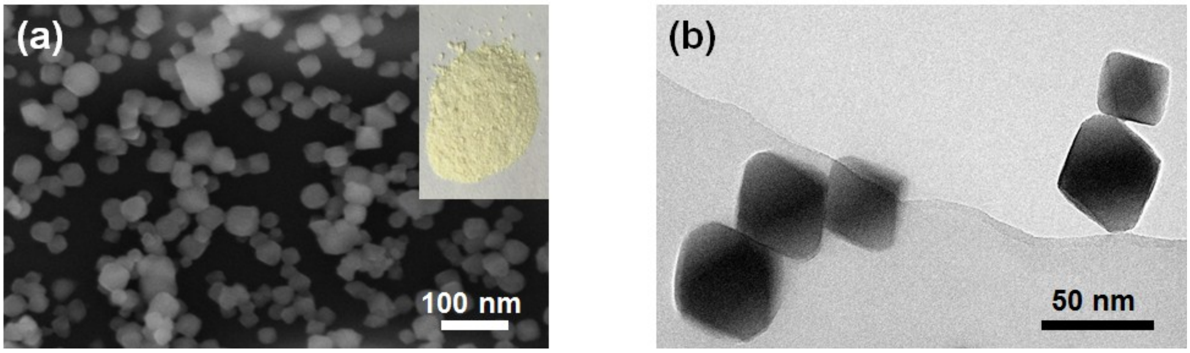

Fig. S1 (a) SEM and (b) TEM images of UiO-66-NH_2。

3. SEM image of Co(II)+Thu@UiO-66-NH_2.

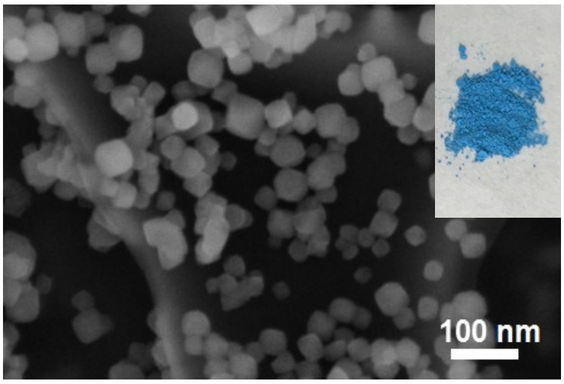

Fig. S2 SEM image and photograph (Inset) of UiO-66-NH_2 mixture with Thu and $CoCl_2$ after being stirred for 8 h.

4. XRD pattern of UiO-66-NH_2 and its corresponding complex with $CoCl_2$ and Thu.

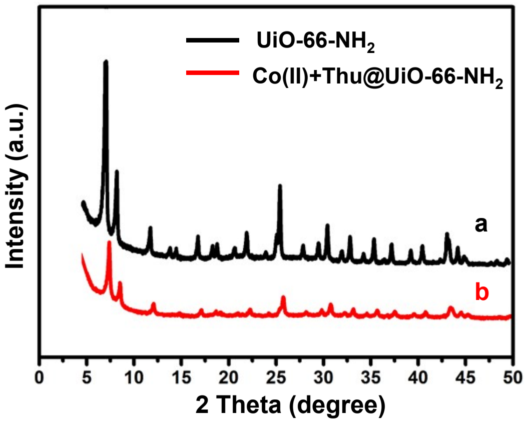

Fig. S3 XRD pattern of (a) UiO-66-NH_2 and (b) Co(II)+Thu@UiO-66-NH_2.

5. SEM images of Co$_9$S$_8$@CTs via pyrolysis under different temperatures

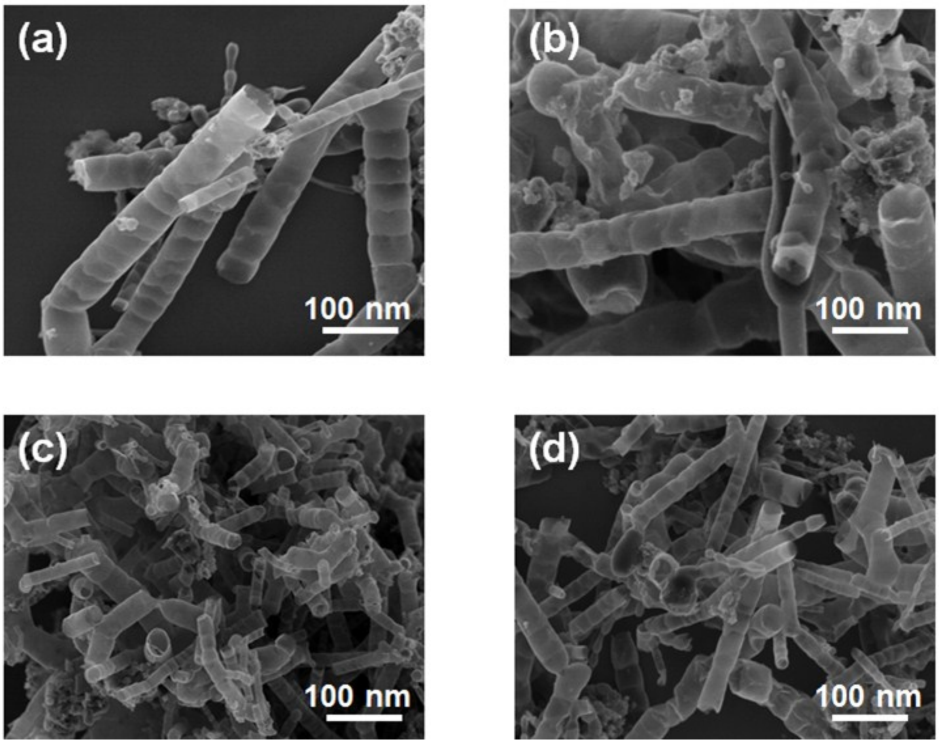

Fig. S4 SEM images of Co$_9$S$_8$@CTs via pyrolysis under different temperatures: (a) 600 ^{o}C, (b) 700 ^{o}C, (c) 900 ^{o}C, and (d) 1000 ^{o}C.

6. Raman spectra of Co_9S_8@CTs via pyrolysis at 800 °C with different molar ratio

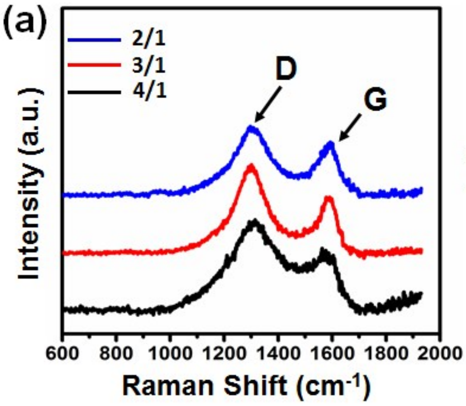

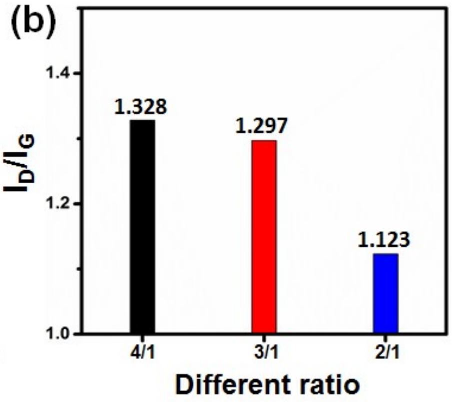

Fig. S5 (a) Raman spectra of Co_9S_8@CTs via pyrolysis at 800 °C with different molar ratio of Thu to $CoCl_2$, and (b) I_D/I_G ratios of various Co_9S_8@CTs materials with different molar ratio.

7. EDX pattern of Co_9S_8@CT-800.

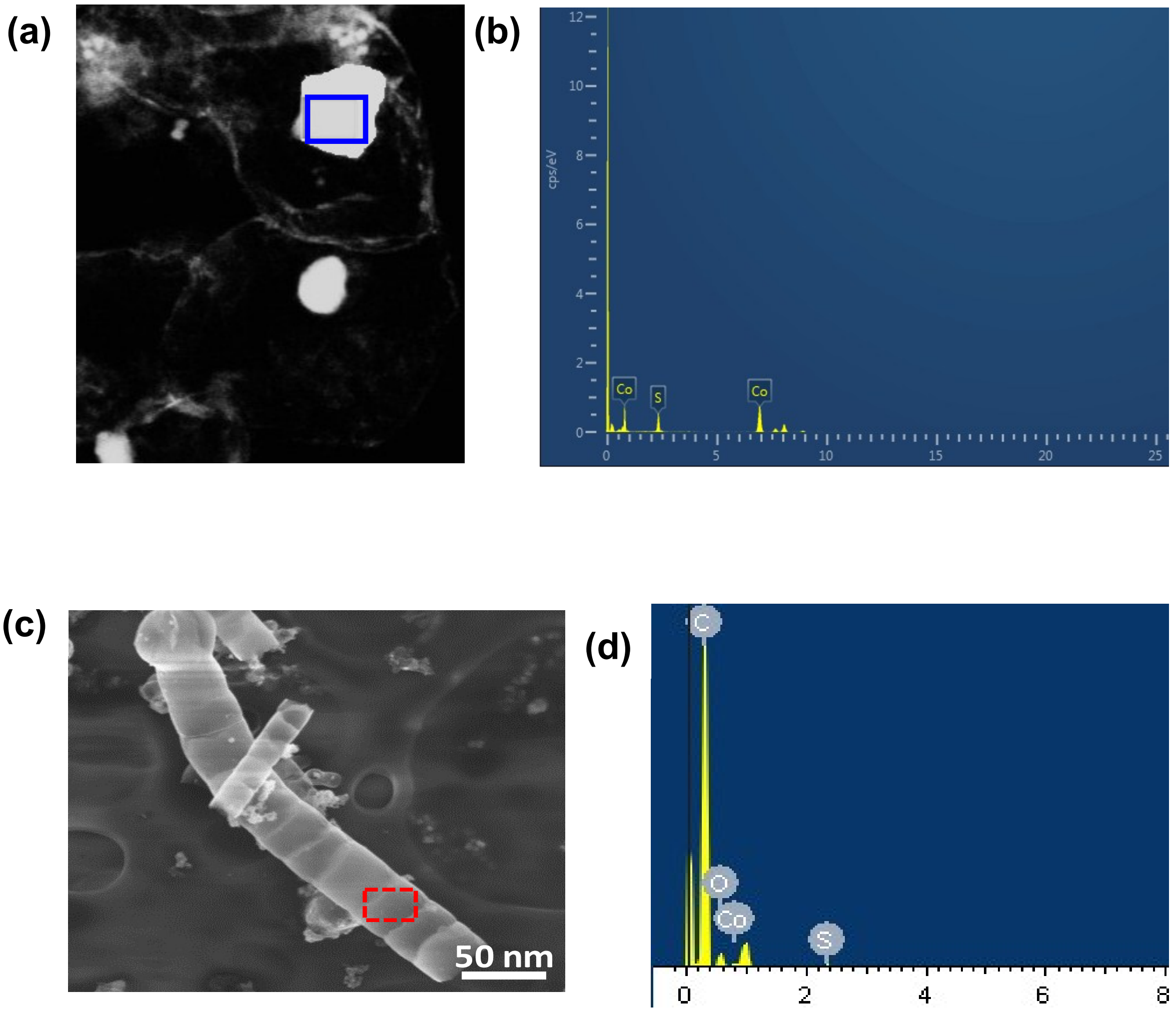

Fig. S6 (a) TEM image of Co_9S_8@CT-800, and (b) the EDX pattern of Co_9S_8@CT-800 in the blue square in (a). (c) SEM image of Co_9S_8@CT-800, and (d) the EDX pattern of Co_9S_8@CT-800 in the red square in (c).

8. Different atomic ratio of Co_9S_8@CTs

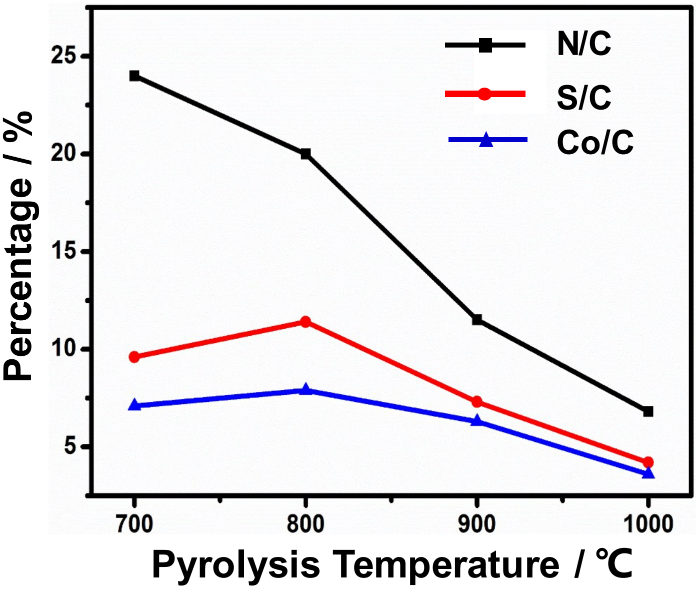

Fig. S7 Different atomic ratio of Co_9S_8@CTs collected from Fig. 2d.

9. High-resolution XPS spectra of Co_9S_8 @CTs.

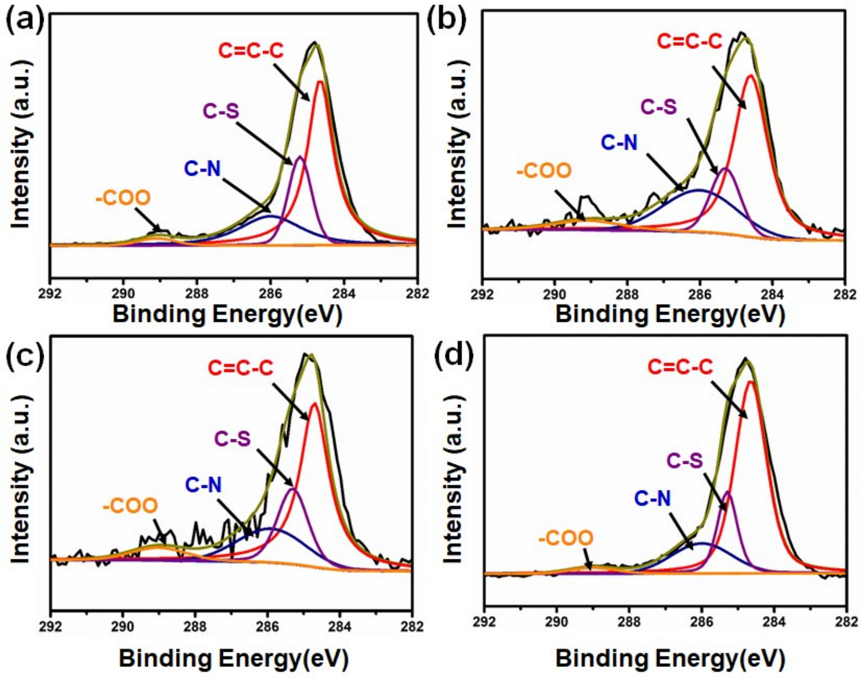

Fig. S8 High-resolution C1s XPS spectra of (a) Co_9S_8@CT-700 °C, (b) Co_9S_8@CT-800 °C, (c) Co_9S_8@CT-900 °C and (d) Co_9S_8@CT-1000 °C.

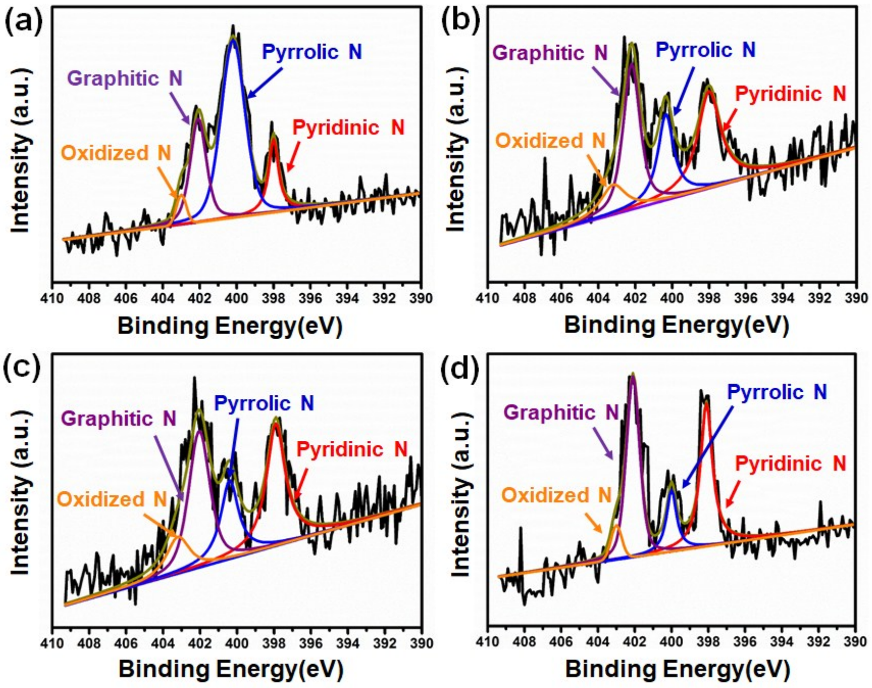

Fig. S9 High-resolution N1s XPS spectra of (a) Co_9S_8@CT-700 °C, (b) Co_9S_8@CT-800 °C, (c) Co_9S_8@CT-900 °C and (d) Co_9S_8@CT-1000 °C.

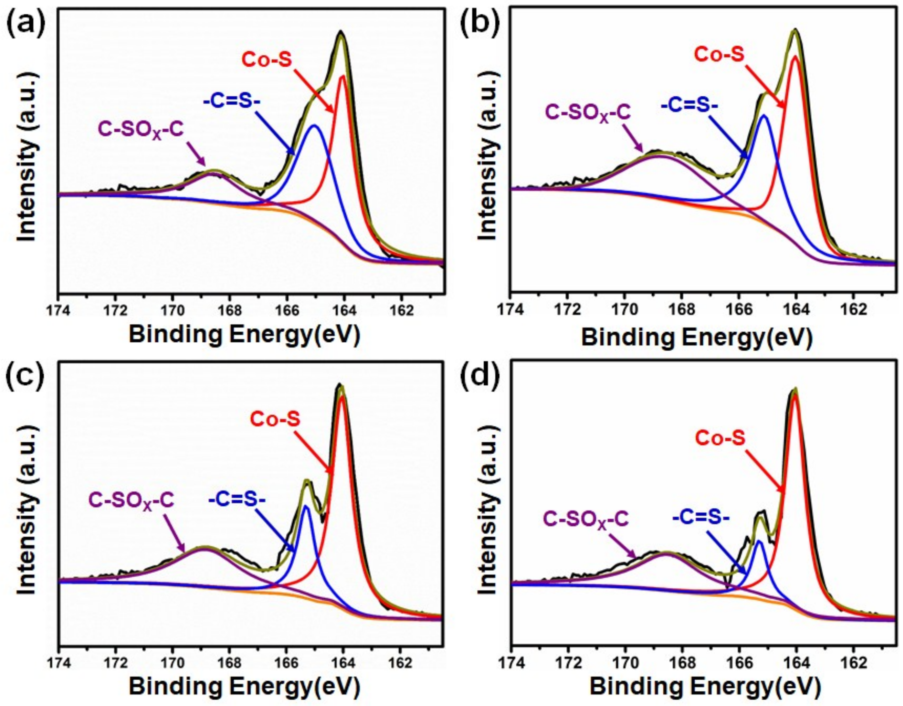

Fig. S10 High-resolution S 2p XPS spectra of (a) Co_9S_8@CT-700 °C, (b) Co_9S_8@CT-800 °C, (c) Co_9S_8@CT-900 °C and (d) Co_9S_8@CT-1000 °C.

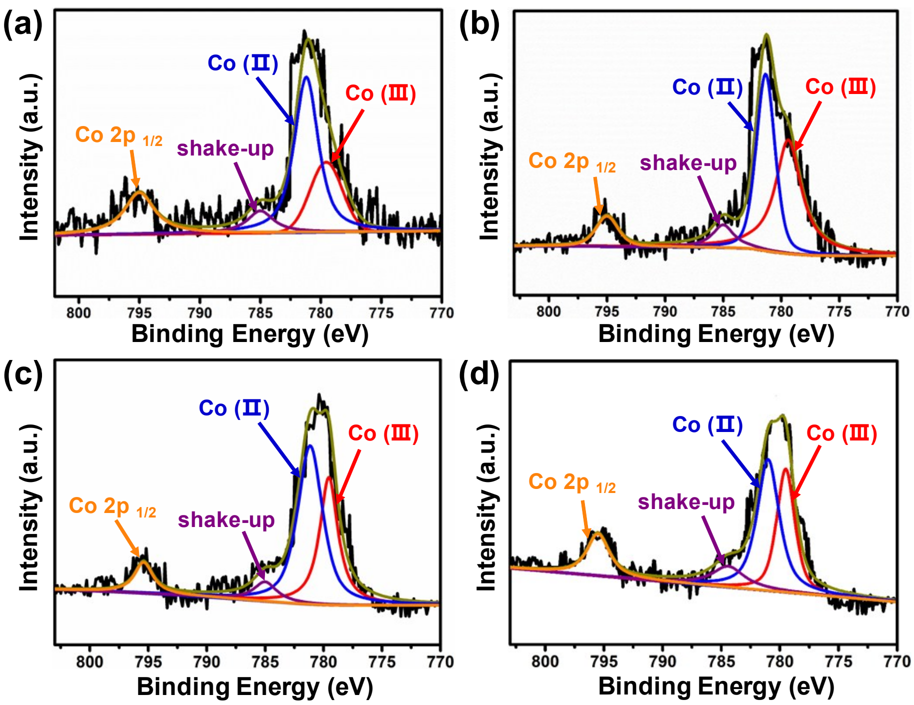

Fig. S11 High-resolution Co 2p XPS spectra of (a) Co_9S_8@CT-700 °C, (b) Co_9S_8@CT-800 °C, (c) Co_9S_8@CT-900 °C and (d) Co_9S_8@CT-1000 °C.

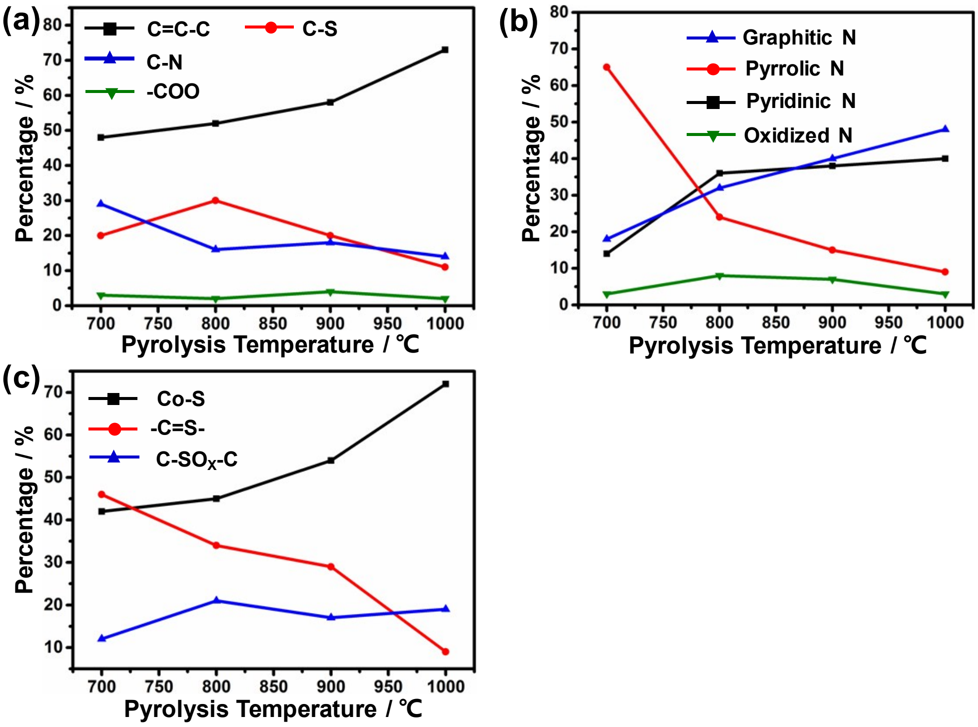

Fig. S12 Comparison of the percentages of the (a) C, (b) N, and (c) S species present in Co_9S_8@CTs as a function of their pyrolysis temperatures.

10. SEM images of blank UiO-66-NH_2, and the UiO-66-NH_2 encapsulated-Thu (or $CoCl_2$) alone via pyrolysis at 800 °C.

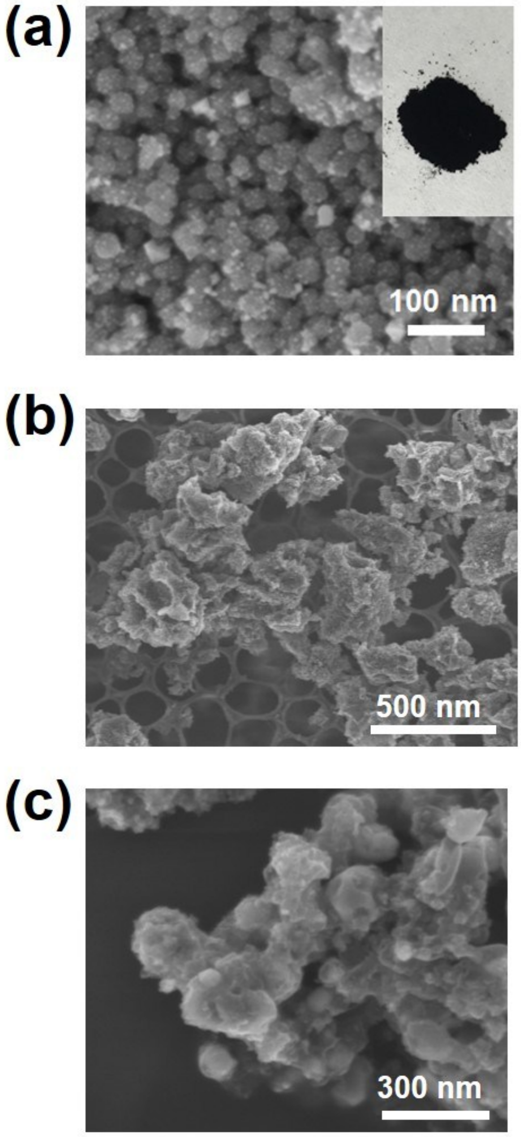

Fig. S13 SEM images of (a) blank UiO-66-NH_2, (b) the UiO-66-NH_2 encapsulated-Thu, and (c) the UiO-66-NH_2 encapsulated-$CoCl_2$ alone via pyrolysis at 800°C.

11. N_2 sorption isotherms of Co_9S_8@CTs at 77 K

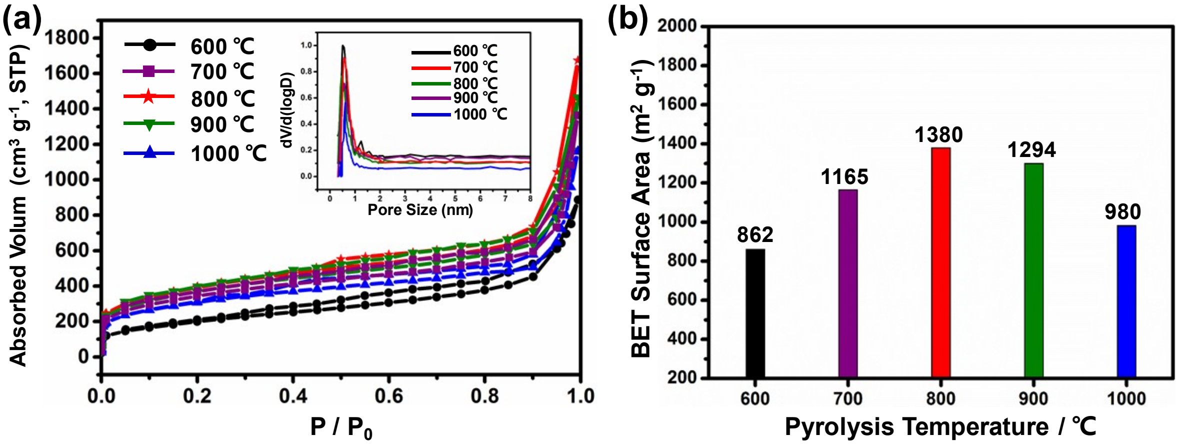

Fig. S14 (a) N_2 adsorption-desorption isotherms of Co_9S_8@CTs materials and (b) the corresponding BET surface areas obtained from (a).

12. LSVs obtained at Co_9S_8@CTs with different temperatures.

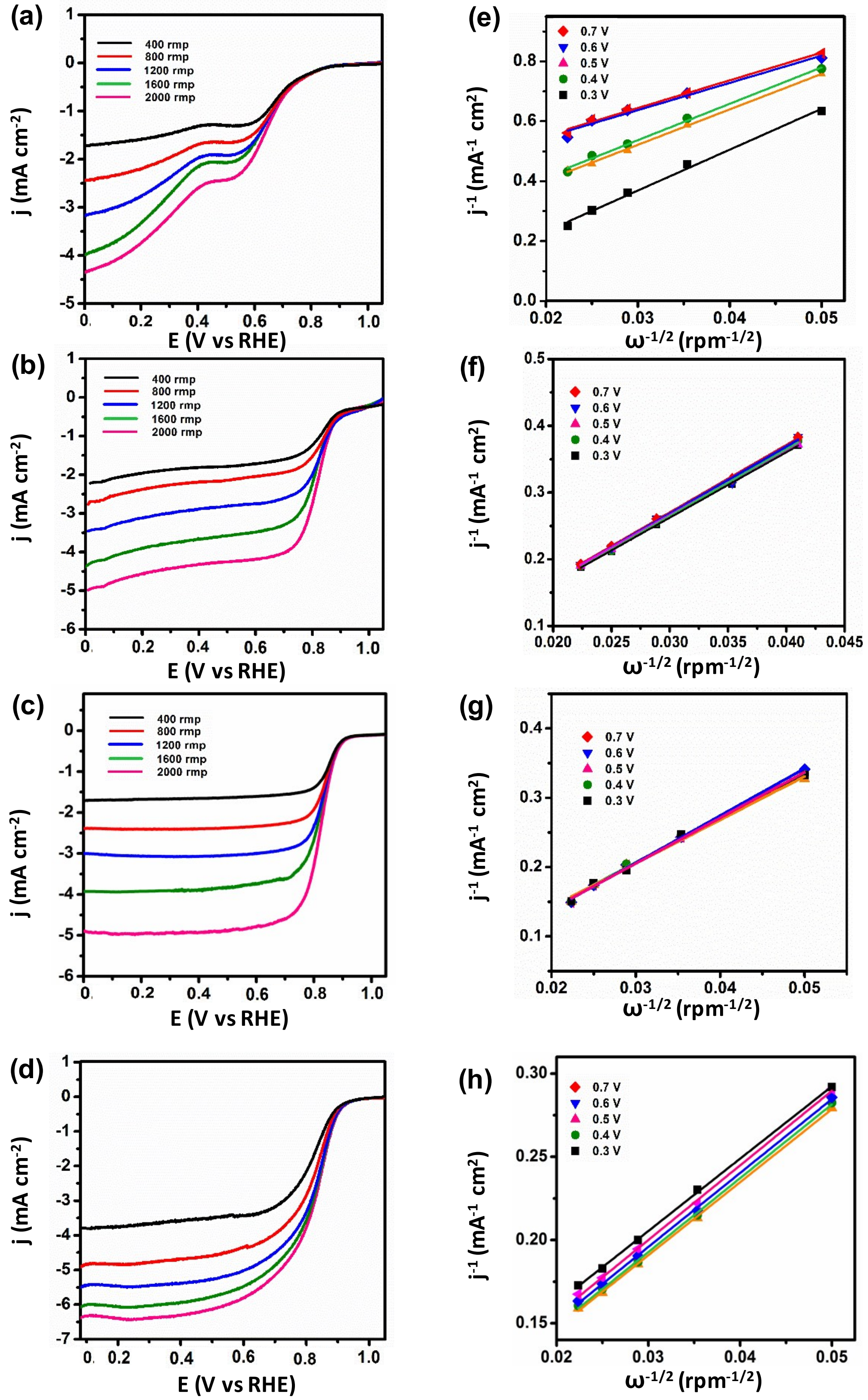

Fig. S15 LSVs at different rotating speeds (a-d) and corresponding K-L plots (e-h) at various potentials of (a, e) Co_9S_8@CT-600, (b, f) Co_9S_8@CT-700, (c, g) Co_9S_8@CT-900, (d, h) Co_9S_8 @CT-1000.

13. LSV curves of UiO-66-800 under different rotating speeds

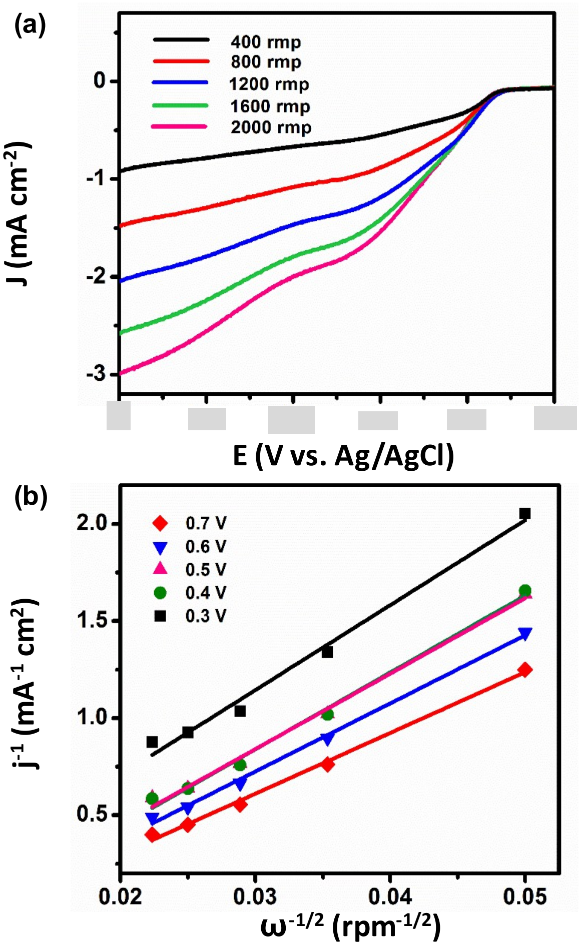

Fig. S16 (a) LSV curves of UiO-66-800 under different rotating speeds, and (b) their corresponding K-L plots.

14. Effect of loading amount on electrocatalytic performance for ORR.

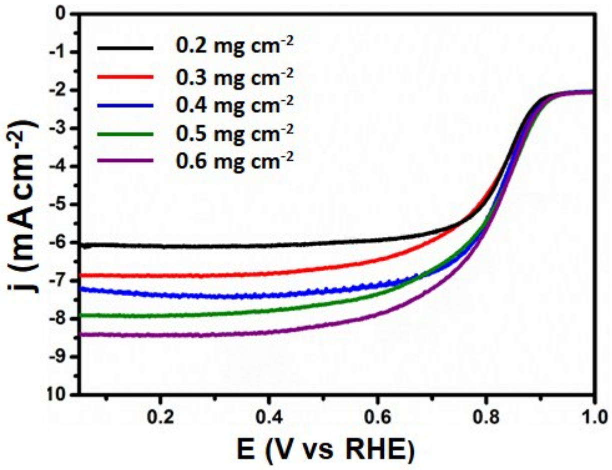

Fig. S17 LSVs obtained at Co_9S_8@CT-800 with different loading amount on the glassy carbon electrode in O_2-saturated 0.1 M KOH at 10 mV s^{-1} with a rotating speed of 1600 rpm.

15. The long-term stability and methanol tolerance

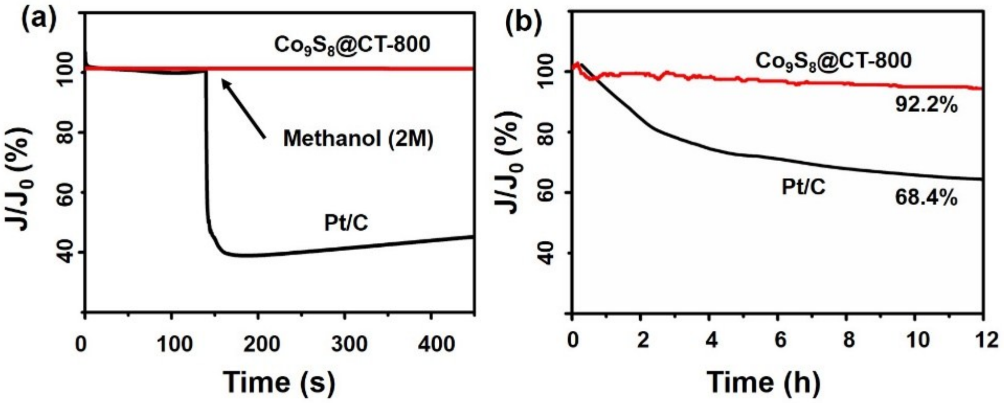

Fig. S18 (a) current-time ($j/j_{0\text{-}t}$) curves for Co_9S_8@CT-800 and Pt/C in O_2-saturated 0.1 M KOH solution with and without 2 M methanol. (b) The stability of Co_9S_8@CT-800 and Pt/C in O_2-saturated 0.1 M KOH solution.

16. The stability for ORR

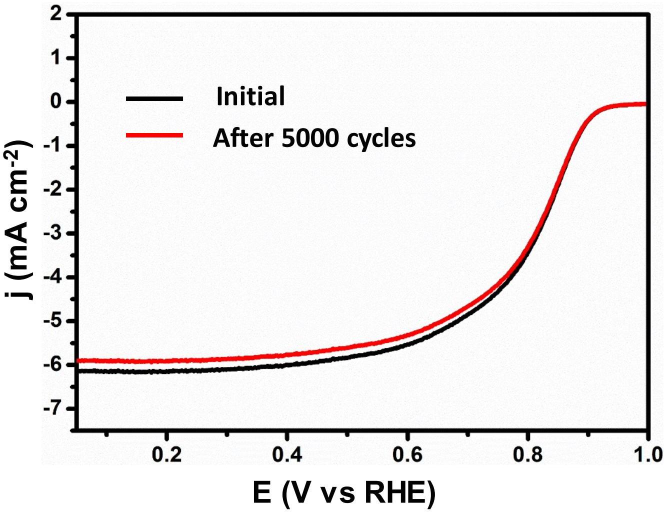

Fig. S19 The stability of Co_9S_8@CT-800 in O_2-saturated 0.1 M KOH at 10 mV s^{-1} after continuous scanning for 5000 cycles with a rotating speed of 1600 rpm.

17. Comparison of the electrocatalytic activity toward ORR.

Table S1. Comparison of the electrocatalytic activity toward ORR of Co_9S_8@CT-800 with others electrocatalysts reported previously.

Catalysts	**Loading (mg cm^{-2})**	**E_0 (V)**	**E_p (V)**	**n**	**Ref**
PANI-Co-C	0.6	0.8	0.75	N/A	S8
CNT/graphene hybrid	0.49	0.89	0.76	4.0	S9
CNTs/carbon hybrid	0.6	0.92	0.82	3.8	S10
Graphene/Co_3O_4	0.6	0.95	N/A	3.9	S11
Co_3O_4/N-rmGO	0.18	0.88	0.83	3.9	S12
N-doped graphene/metals	0.6	0.94	N/A	3.95	S13
N-doped carbon frameworks	0.1	0.79	0.79	3.95	S14
graphene-MOF composite	0.16	0.91	N/A	3.82	S15
MOF-derived carbons	0.2	0.9	N/A	3.61	S16
ZIF-derived porous carbons	0.34	0.9	0.76	3.9	S17
P-doped ZIF8-derived carbons	0.1	0.9	0.71	4.0	S18
Sulphur-doped graphene	0.09	0.88	0.66	3.13	S19
N-Co_9S_8/G	0.5	0.91	N/A	3.96	S20
Fe-N-CNT-OPC	0.4	0.89	N/A	3.99	S21
Co_9S_8@CT-800	0.2	0.92	0.86	4.0	The present work

N/A: not mentioned

18. Effect of loading amount on electrocatalytic performance for OER.

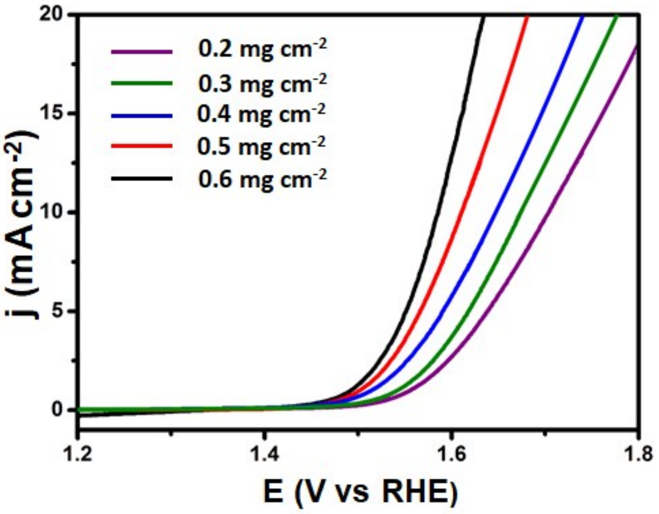

Fig. S20 LSVs obtained at Co_9S_8@CT-800 for OER with different loading amounts on the glassy carbon electrode in in O_2-saturated 0.1 M KOH at 10 mV s^{-1} with a rotating speed of 1600 rpm.

19. The optimized N-doped graphene.

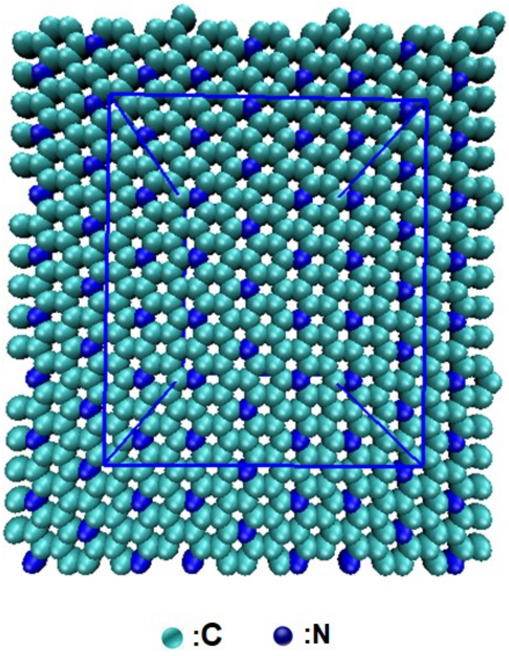

Fig. S21 The optimized N-doped graphene.

20. Three representative V_CN, V_N, and V_C, and corresponding Co_9S_8 adsorption models.

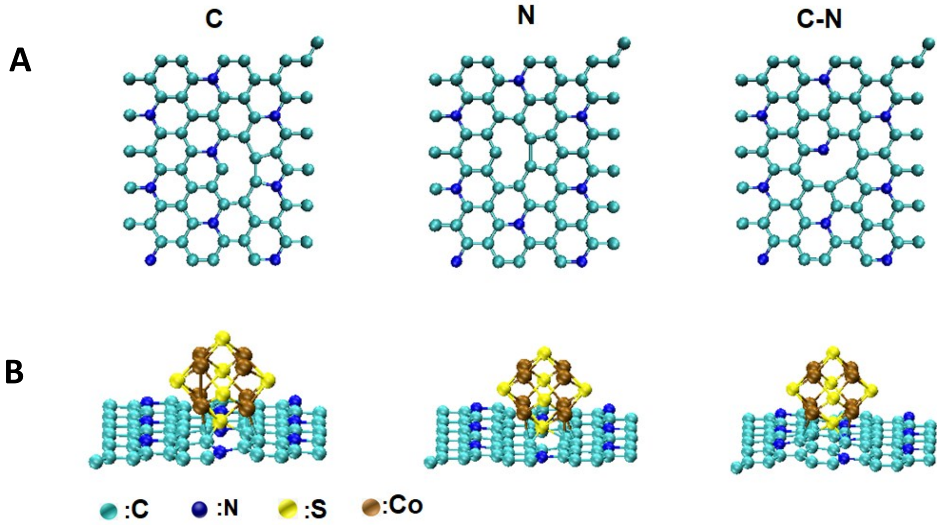

Fig. S22 (A) Three representative V_C, V_N, and V_CN and (B) corresponding Co_9S_8 adsorption models (from left to right).

21. Free energy diagrams for V_CN, and V_C corresponding Co$_9$S$_8$ adsorption models.

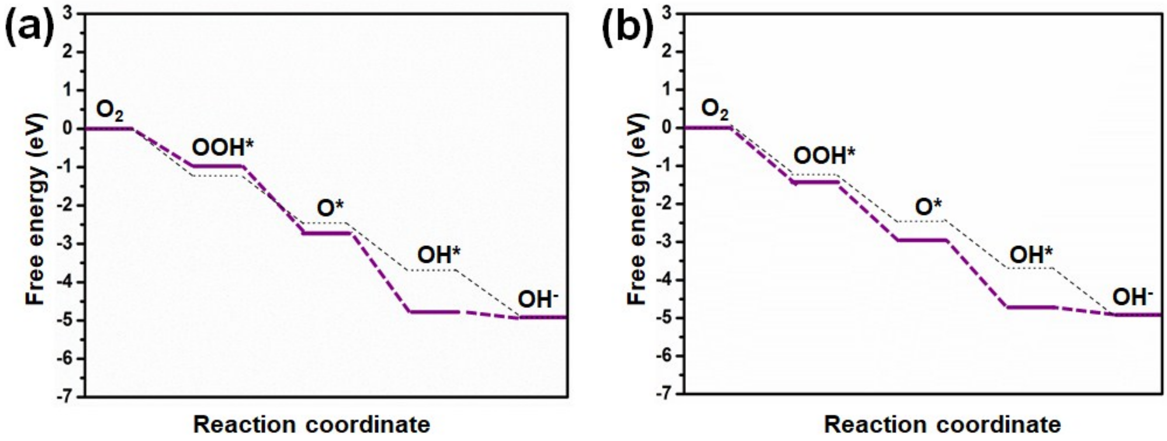

Fig. S23 Free energy diagrams for (a) V_CN and (b) V_C pathway on Co$_9$S$_8$@CT-800 in alkaline solution, respectively. * stands for the adsorbed intermediates. Solid lines show calculated values, dashed lines represent the energy profile of an ideal catalyst.

22. Free energy diagrams at S site of Co$_9$S$_8$@CT-800

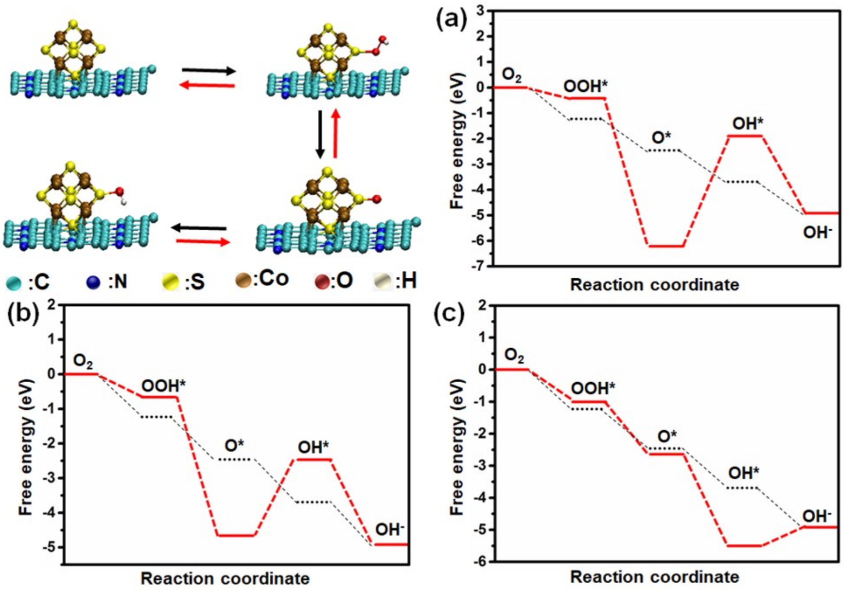

Fig. S24 Free energy diagrams for (a) V_C, (b) V_N, and (c) V_CN pathway on S site of Co$_9$S$_8$@CT-800 in alkaline solution, respectively. *stands for the adsorbed intermediates. Solid lines show calculated values, dashed lines represent the energy profile of an ideal catalyst.

23. The contribution of entropy and heat capacity to the free energy

Explanation S1.

In our system, the Gibbs free energy is calculated using

$$G = E_{DFT} + ZPE - TS + C_vT \qquad (S2)$$

where G is Gibbs free energy, E_{DFT} the electronic energy from DFT calculations, ZPE is zeropoint-energy, S is entropy, and C_v is heat capacity, T is temperature. According to Equation (S2), the dependence of value of entropy (S) and heat capacity (C_v) on Gibbs free energy (G) value is related to the temperature (T). In the case of the Co_9S_8/ N- graphene model, the S and C_v values are calculated to be 0.845 KJ/mol K, and 0.835 KJ/mol K, respectively. When the temperature was changed by 100 K, the energy difference was calculated to be ~

-0.93 meV, which is negligible to the energy change in the whole system. These results demonstrate that the temperature effect on the DFT model in our system is negligible.

24. References for Supporting Information

S1. J. Hutter, M. Lannuzzi, F. Schiffmann, J. Vandevondele. *Wires Comput. Mol. Sci.* 2014, **4**, 15.

S2. J. P. Perdew, K. Burke, M. Ernzerhof. *Phys. Rev. Lett.* 1996, **77**, 3865.

S3. S. Grimme. *J. Comput. Chem.* 2006, **27**, 1787.

S4. J. Vandevondele, J. Hutter. *J. Chem. Phys.* 2007, **127**, 114105.

S5. J. Vandevondele, M. Krack, F. Mohamed, M. Parrinello, T. Chassaing, J. Hutter. *Comput. Phys. Commun.* 2005, **167**, 103.

S6. S. Goedecker, M. Teter, J. Hutter. *Phys. Rev. B* 1996, **54**, 1703.

S7. C. Hartwigsen, S. Goedecker, J. Hutter. *Phys. Rev. B* 1998, **58**, 3641.

S8. G. Wu, K. L. More, C. M. Johnston, P. Zelenay. *Science* 2011, **332**, 443.

S9. Y. Li, W. Zhou, H. Wang, L. Xie, Y. Liang, F. Wei, J-C. Idrobo, S. J. Pennycook, H. Dai. *Nat. Nanotech*. 2012, **7**, 394.

S10. Y. J. Sa, C. Pak, H. Y. Jeong, S-H. Park, Z. Lee, K. T. Kim, G-G, Park, S. H. Joo. *Angew. Chem. Int. Ed.* 2014, **53,** 4102.

S11. S. Li, D. Wu, C. Chen, J. Wang, F. Zhang, Y. Su, X. Feng. *Angew. Chem. Int. Ed.* 2013, **52**, 12105.

S12. Y. Liang, Y. Li, H. Wang, J. Zhou, J. Wang, T. Regier, H. Dai. *Nat. Mater*. 2011, **10**, 780.

S13. W. Wei, H. Liang, K. Parvez, X. Zhuang, X. Feng, K. Miillen. *Angew. Chem. Int. Ed.* 2014, **53**, 1570.

S14. H. W. Liang, W. Wei, Z-S. Wu, X. Feng, K. Müllen. *J. Am. Chem. Soc.* 2013, **135**, 16002.

S15. M. Jahan, Q. Bao, K. P. Loh. *J. Am. Chem. Soc.* 2012, **134**, 6707.

S16. Z. Xiang, Y. Xue, D. Cao, L. Huang, J-F. Chen, L. Dai. *Angew. Chem. Int. Ed*. 2014, **53**, 2433.

S17. H-X. Zhong, J. Wang, Y-W. Zhang, W-L. Xu, W. Xing, D. Xu, Y-F. Zhang, X-B. Zhang. *Angew. Chem. Int. Ed.* 2014, **53**,14235.

S18. W. Zhang, Z-Y. Wu, H-L. Jiang, S-H. Yu. *J. Am. Chem. Soc*. 2014, **136**, 14385.

S19. Z. Ma, S. Duo, A. Shen, L. Tao, L. Dai, S. Wang. *Angew. Chem. Int. Ed*. 2015, **54**,1888.

S20. S. Duo, L. Tao, J. Huo, S. Wang, L. Dai. *Energy Environ. Sci*. 2016, **9**, 1320.

S21. J. Liang, R. F. Zhou, X. M. Chen, Y. H. Tang, S. Z. Qiao. *Adv. Mater*. 2014, **26**, 6074.